J. Fluid Mech. (1999), *vol.* 383, *pp.* 285–305. Printed in the United Kingdom

Incipient breaking of steady waves in the presence of surface wakes

By MATTHEW MILLER[1], TOBIAS NENNSTIEL[2], JAMES H. DUNCAN[1], ATHANASSIOS A. DIMAS[1], AND STEPHAN PRÖSTLER[2]

[1]Department of Mechanical Engineering, University of Maryland, College Park, MD 20742, USA

[2]Lehrstuhl A für Thermodynamik, Technische Universität München, Boltzmannstr 15, 85748 Garching, Germany

(Received 5 March 1998 and in revised form 8 October 1998)

The effect of free-surface drift layers on the maximum height that a steady wave can attain without breaking is explored through experiments and numerical simulations. In the experiments, the waves are generated by towing a two-dimensional fully submerged hydrofoil at constant depth, speed and angle of attack. The drift layer is generated by towing a plastic sheet on the water surface ahead of the hydrofoil. It is found that the presence of this drift layer (free-surface wake) dramatically reduces the maximum non-breaking wave height and that this wave height correlates well with the surface drift velocity. In the simulations, the inviscid two-dimensional fully nonlinear Euler equations are solved numerically. Initially symmetric wave profiles are superimposed on a parallel drift layer whose mean flow characteristics match those in the experiments. It is found that for large enough initial wave amplitudes a bulge forms at the crest on the forward face of the wave and the vorticity fluctuations just under the surface in this region grow dramatically in time. This behaviour is taken as a criterion to indicate impending wave breaking. The maximum non-breaking wave elevations obtained in this way are in good agreement with the experimental findings.

1. Introduction

The steady free-surface flow field generated by a ship moving at constant speed in calm water typically includes breaking waves at the bow and the stern. The bow wave and the parts of the stern wave far from the ship track propagate in undisturbed water while the parts of the stern wave near the ship track propagate in a flow with a free-surface shear layer due to the boundary layer of the hull and/or the surface wakes of upstream breaking waves (surface wakes of steady breaking waves have been studied by Battjes & Sakai 1981 and Duncan 1981, 1983). A comprehensive theoretical or numerical model of wave breaking in the presence of surface wakes must include information on incipient wave breaking conditions. An incipient breaking wave is defined as a non-breaking wave for which even a slight increase in its steepness would cause breaking. The fact that upstream surface wakes affect the incipient breaking conditions of downstream waves is demonstrated by observations that the breaking stern wave crest frequently extends out past the side of the ship to a width equal to the width of the breaking bow wave, even when the stern wave steepness appears to

be very low in terms of calm water incipient breaking conditions. These effects are illustrated in the photograph shown on the cover of Parker (1994).

The incipient breaking condition for steady waves in calm water was explored theoretically by Stokes (1847). In this work, it was assumed that at incipient breaking the fluid velocity at the crest of the wave approached the phase speed of the wave. Thus, using Bernoulli's equation for a streamline on the free-surface and assuming constant pressure on this streamline, the incipient breaking amplitude of a steady wave is given by

$$\zeta_{max} = \frac{U_\infty^2}{2g}, \tag{1.1}$$

where ζ_{max} is the height of the crest above the mean water level, U_∞ is the wave phase speed, and g is the acceleration due to gravity. Stokes also found, using irrotational flow theory, that the incipient breaking wave would have a sharp crest with an included angle of 120°. Subsequent studies have shown that it is nearly impossible to obtain the above wave form either in nature or in the laboratory owing to instabilities which set in at smaller wave amplitudes.

The effect of a uniform vorticity distribution on the shape of the crests of limiting wave forms was investigated with a two-dimensional inviscid theory by Miche (1944). It was found that the crest is symmetric and sharp with an included angle of 120° as in the case without vorticity. However, when the surface drift is in the same direction as the wave propagation, the front and rear wave faces at the crest have a finite upward curvature which is not present in the irrotational case.

The effect of a thin surface wind drift layer upon the incipient breaking condition was investigated by Banner & Phillips (1974). A steady theory was used in which, in the same manner as Stokes, incipient breaking was assumed to occur when the fluid velocity at the crest equalled the wave phase speed. However, in the presence of a wind drift layer with the surface drift velocity (relative to the fluid at infinite depth) in the same direction as the wave phase speed, the incipient breaking condition occurs at smaller wave amplitudes than predicted by Stokes:

$$\zeta_{max} = \frac{U_\infty^2}{2g}(1-q)^2, \tag{1.2}$$

where $q = (U_\infty - U(0))/U_\infty$, where $U(0)$ is the fluid velocity at the water surface in the reference frame of the wave crest but with no wave present. This effect on the limiting wave amplitude was also mentioned qualitatively by Miche (1944) for the case of uniform vorticity. In (1.2), the result of Stokes is reproduced when $q = 0$. For the case of ship waves, the wind drift layer would be replaced by the wake from an upstream breaker or the ship hull.

Computations of waves propagating in the presence of free-surface shear layers have been reported by Simmen & Saffman (1985) and Teles Da Silva & Peregrine (1988). In Simmen & Saffman (1985), waves on a fluid with constant vorticity and infinite depth were considered, while in Teles Da Silva & Peregrine (1988) waves on a layer of fluid with constant vorticity and finite depth were considered. In both cases, wave profiles, extreme wave heights and wave propagation speeds were presented.

Experimental studies of the incipient breaking conditions for steady two-dimensional waves generated in calm water have been reported by Salvesen & von Kerczek (1976, see also Salvesen 1981) and Duncan (1983). In both studies, the waves were generated with a submerged hydrofoil moving at constant speed, depth, and angle of attack in a towing tank. In Salvesen & von Kerczek (1976), the incipient breaking condition

was determined by fixing the depth and angle of attack of the foil and varying the foil speed from one experimental run to another. At low speeds, the wave steepness was small and no breaking occurred. As the speed was increased, the wave became steeper and, for a high enough speed, the wave broke. If the foil speed was increased past this point, the breaking eventually stopped. Thus, speeds just less than the speed for which breaking started and just high enough for breaking to stop were chosen and the wave slope was measured at each of these incipient breaking conditions. This procedure was repeated for several depths of submergence. The maximum surface slope of these incipient breaking waves varied from 11° to 25° and did not show any consistent trend. Duncan (1983) found that for fairly steep non-breaking waves, breaking could be triggered by dragging a cloth for 1 or 2 s on the water surface ahead of the wave. For small enough wave steepnesses, when the cloth was removed, the wave would stop breaking. However, for higher wave steepnesses the wave would continue to break after the cloth was removed. The wave profiles measured at the incipient breaking condition determined by whether or not the wave would continue breaking when the cloth was removed were very consistent. The maximum slope of each profile was found to be about 16°; this value increased slowly with towing speed. Even though the cloth was used momentarily to trigger breaking, the above defined incipient breaking condition is for a wave in calm water. These simple experiments also indicated that for steepnesses a little greater than the above defined incipient breaking steepness, the flow could exist in either a breaking or non-breaking state.

In the present paper, the effect of a steady surface wake on the incipient breaking condition of a steady wave is examined experimentally and numerically. In the experiments, a plastic sheet is dragged along the water surface at a fixed distance ahead of the steady wave created by a towed hydrofoil. Unlike the experiments of Duncan (1983) where the cloth was only dragged on the water surface for a short time to get breaking started and then removed so that the wave continued to propagate in calm water, in the present experiments the plastic sheet was always present in front of the wave. With the hydrofoil at a fixed depth of submergence (one for which it produces a non-breaking wave in calm water), the distance, Δx, between the trailing edge of the plastic sheet and the hydrofoil was varied to obtain the incipient breaking condition. For small Δx, the local surface drift near the wave crest, q, is high and the wave tends to break even when its amplitude is small. For large Δx, q is small and the wave does not break, as if it were propagating in calm water. The incipient breaking wave was taken as the non-breaking wave for which breaking will start if Δx is decreased by a small amount. Wave profile measurements are taken at the incipient breaking conditions and the wakes of the plastic sheets are characterized through measurements of the mean horizontal velocity distributions taken at three streamwise locations for each of two plastic sheets. These measurements are used to quantify the effect of q and the wake momentum thickness on the incipient breaking conditions. Numerical simulations of a similar flow are performed using a fully nonlinear inviscid two-dimensional free-surface flow code. The incipient breaking conditions found in the experiments are compared to the theory of Banner & Phillips (1974) and to the results of the numerical simulations. The experimental data and the numerical results are further used to explore the physics of the instability processes at the incipient breaking condition.

The remainder of this paper is divided into five sections. In § 2, the details of the experimental setup and measurement techniques are presented. This is followed in § 3 by a description of the experimental results. In § 4, the numerical model is presented

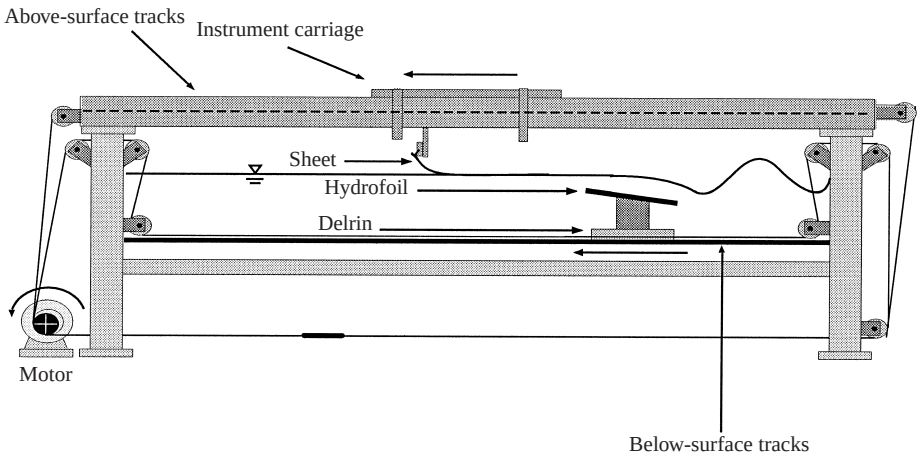

FIGURE 1. Side view of the towing tank.

along with some typical results. The experimental and numerical results are compared and discussed in § 5. Finally, the conclusions are presented in § 6.

2. Experimental techniques

2.1. *The towing tank*

The experiment was performed in a towing tank with dimensions of 14.8 m long, 1.22 m wide and 1.0 m deep, see figure 1. The sidewalls of the tank are made of glass to allow flow visualization and optical measurements. The tank contains both below-surface and above-surface towing systems. The below-surface towing system includes two fully submerged 'L'-shaped tracks that are mounted near each of the sidewalls. Objects are towed along the tracks by two stainless steel wire ropes which enter the water at one end of the tank and leave from the other end. Thus, no part of the towing system breaks the water surface in the vicinity of the towed object. The wire ropes are driven by a servo motor mounted at one end of the tank, see figure 1. The above-surface towing system uses two tracks mounted above the tank, one near each sidewall. These tracks consist of a 3.8 cm diameter stainless steel precision rod on one side and a 5.1×5.1 cm precision-ground steel I-beam on the other, see figure 2. An instrument carriage rides on the tracks via four hydrostatic oil bearings. When high-pressure oil is supplied to the bearings, a thin film of oil is forced between the bearings and the tracks, thereby greatly reducing vibration and friction levels of the carriage. The carriage is driven by two separate wire ropes which are powered by the same servo motor that powers the below-surface towing system. Precise towing speeds are obtained by means of a computer-based feedback control system. The towing speed is verified with an independent measurement obtained from two timing switches located 209.87 cm apart and connected to a timer with nanosecond accuracy.

In the present experiments, steady waves were generated with a hydrofoil mounted on the below-surface towing system. The hydrofoil is an aluminium NACA 0012 airfoil with a 20 cm chord which is operated at a 9° angle of attack. This foil spans the width of the tank with a small clearance of 1.4 cm between the edges of the foil and the walls of the tank. The foil is mounted on two stainless steel plates which, in turn, are mounted on two Delrin blocks, each with a groove cut into it, see figure

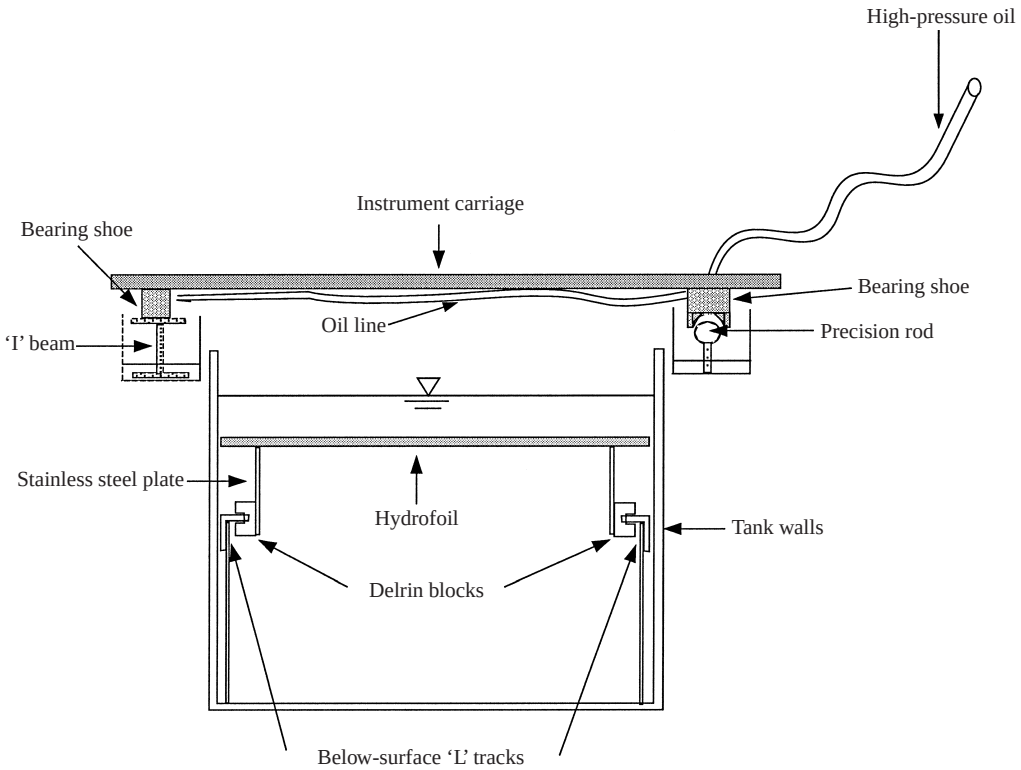

FIGURE 2. End view of the towing tank.

	Short	Long
Length (cm)	63.5	101.6
Width (cm)	101.6	114.3
Contact length (cm)	56	94

TABLE 1. Physical dimensions of the short and long Mylar sheets.

2. These grooves provide a low-friction bearing surface to slide along the submerged L-shaped tracks. The surface wake was created with sheets of Mylar dragged along the surface of the water at a fixed distance ahead of the hydrofoil. The Mylar sheets have a thickness of 0.13 mm and a specific gravity of 1.25. Although these sheets are heavier than water, the contact angle at the Mylar–air–water interface around the edges of the sheets allowed them to remain on the water surface. Two Mylar sheets were utilized, each having the physical dimensions as shown in table 1. As can be seen from the table, the sheet widths are not equal and do not completely span the width of the wave tank; however, since both widths are greater than two lengths of the gravity wave (about 40 cm) the variation of the sheet width has no noticeable effect on the results.

The mounting assembly used to hold the Mylar sheets in place was attached to the instrument carriage via two linear motion slides to allow for vertical positioning of the entire assembly, see figure 3. Attached to these slides was a long flat bar and a long 90° angle, both spanning the width of the tank. The Mylar sheet was inserted between the bar and the angle, then the two were clamped together holding the sheet

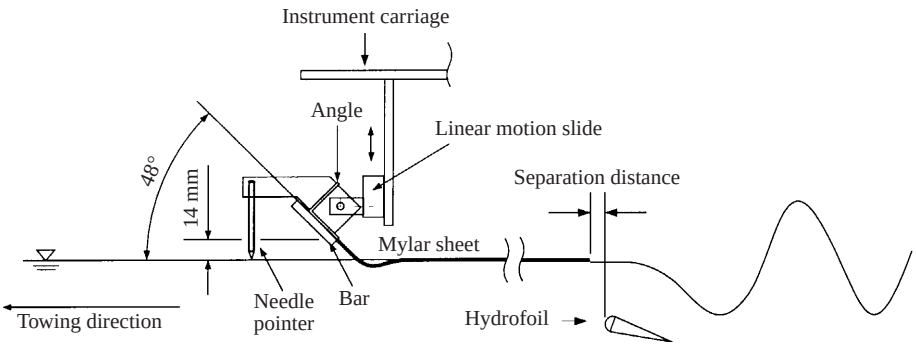

FIGURE 3. Side view of mounting assembly for Mylar sheets.

in place. To create a two-dimensional wake, the contact area between the sheet and the water surface must be rectangular. The driving factor needed to maintain this rectangular form is a straight waterfront at the leading edge of the contact area. The angle and height of the bar relative to the water surface were adjusted to maintain this straight, repeatable waterfront. By trial and error, the angle of the bar to the water surface was chosen to be 48°. One needle pointer is mounted on each end of the bar perpendicular to the water surface. These pointers are used to maintain a repeatable distance between the mounting assembly and the water surface. The relative position between the above-surface carriage and hydrofoil is adjustable. This allows the separation distance between the trailing edge of the Mylar sheet and the leading edge of the hydrofoil to be varied. Towed by itself, the sheet created a wake at the water surface and as discussed below, a train of small-amplitude waves.

In order to control water clarity and surfactants, a recirculating skimmer system was used. This system includes two surface skimmers located at one end of the tank. The water from the skimmers was sent to a diatomaceous-earth filter and then sent back to the tank through a port at the opposite end of the tank from the skimmers. When fresh water was needed, tap water was sent through a separate filter before entering the tank. The skimming system was run for at least 2 hours and then turned off about 20 min before any of the measurements were taken.

2.2. *Mean velocity measurements*

A rake of three Pitot tubes was used for the mean velocity measurements in the wakes of the Mylar sheets. The rake had a spanwise horizontal spacing between tubes of 10 cm and a vertical spacing of 10 mm. The large horizontal spacing was chosen to minimize the interaction between the individual tubes. The rake was mounted on a telescoping arm which was attached to the instrument carriage, allowing the streamwise distance from the trailing edge of the Mylar sheet to the tips of the tubes to be varied. The Pitot tube rake was attached to the arm via a linear traverser to allow vertical positioning. Each Pitot tube was connected through transparent Tygon tubing to a separate differential diaphragm-type pressure transducer (*Validyne* Model P305D), each having a range of ± 0.2 p.s.i. The three pressure transducers were mounted on the end of the telescoping arm at equal heights above the water surface. The analog voltage output of each pressure transducer was connected to a 12-bit analog-to-digital (A/D) converter operating at 1200 samples per second and the digitized output was stored in the memory of a PC. The signal taken during the steady-state part of each run was then averaged. Division of the full pressure range of the transducer by the resolution of the A/D converter yields an accuracy of

0.1 cm s^{-1} at an average speed equal to the towing speed, 80.5 cm s^{-1}. However, during runs made with the Pitot tubes moving through the undisturbed water in the towing tank, a pressure fluctuation corresponding to a root-mean-square velocity fluctuation of 0.2 cm s^{-1} was observed.

The above-described equipment was used to measure the vertical distribution of mean horizontal velocity at three streamwise locations behind each Mylar sheet. These measurements were performed without the presence of the hydrofoil. In performing these experiments, it was observed that, like the hydrofoil, the Mylar sheets generated a train of two-dimensional surface waves whose phase speed was equal to the towing speed. Though the amplitudes of these waves were small (at most 0.17 cm), they were found to have a noticeable effect on the mean velocity distributions (see below). In order to use the Pitot tubes in locations where the fluid velocity was known to be horizontal, the velocity distributions were measured at the streamwise locations of the troughs of the following wavetrain. For a towing speed of 80.4 cm s^{-1}, visual examination of the wavetrains showed the wavelengths to be about 40 cm; by linear theory with no surface wake the length of this wave would be 41.4 cm. The measurement locations were taken as 38, 80 and 120 cm behind the trailing edge of the short Mylar sheet and 40, 80 and 120 cm behind the trailing edge of the long Mylar sheet.

A mean velocity distribution at one streamwise location was typically measured during the period of 1 day. The first step in the measurement process was to remove air bubbles from the Pitot tubes, tubing and transducers. The next step was to calibrate by running the Pitot tubes at predetermined velocities through the undisturbed water in the towing tank. From each record, the data recorded after a steady state was reached (after about 4 s in each run) were averaged and used to create a calibration curve for the wake flow measurements. Upon completion of the calibration runs, the Mylar sheet was clamped onto the mounting assembly as illustrated in figure 3 and the Pitot tubes were set at one of the three distances from the trailing edge of the Mylar sheets. During each experimental run the depth of the rake was held fixed. This depth was varied in a random manner from run to run until measurements at enough depths were taken to ensure a well resolved profile of the mean velocity; runs at most measurement depths were repeated three times. After running for a period of about 3 hours, the calibration process described above was repeated. The output files from the A/D converter were processed through a computer program to convert the digital points into velocities using the average of the calibrations before and after the data-taking runs. It should be noted that the finite size of the Pitot tubes resulted in an inability to make fluid velocity measurements closer than about 5 mm from the water surface.

A sample of a raw mean velocity distribution is shown in figure 4(*a*). In this figure, a depth of zero is the local free-surface elevation. As can be seen in the plot, the mean velocity increases slowly as the depth decreases from 10 cm to about 2 cm. Thereafter, the velocity decreases rapidly to about 65 cm s^{-1} near the free-surface. The increase in velocity between 10 cm and 2 cm in depth is an effect due to the small-amplitude wavetrain generated by the Mylar sheet. The horizontal velocity distribution in a potential flow wave at its trough can be described by linear wave theory (see for example Lamb 1932):

$$U_w = U_\infty(1 + ak\mathrm{e}^{kz'}), \tag{2.1}$$

where U_∞ is the carriage velocity, a is the wave amplitude, k is the wavenumber given by $k = g/U_\infty^2$ in linear theory, and z' is the vertical coordinate (positive up) relative to

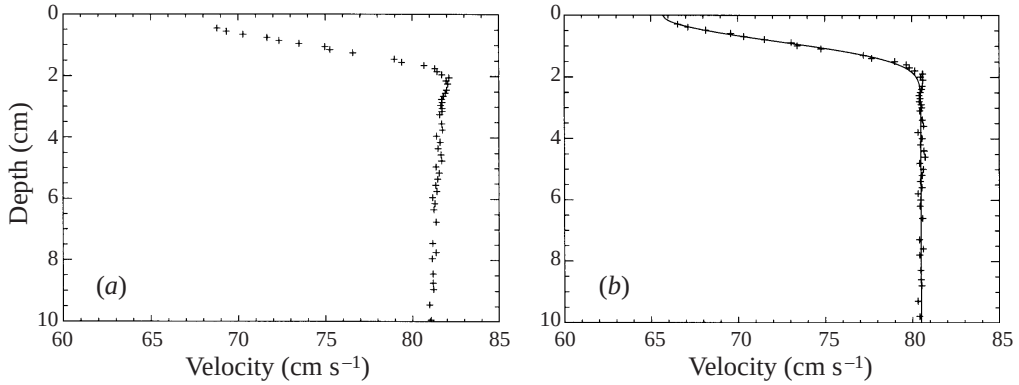

FIGURE 4. Mean horizontal velocity versus depth below the mean free water surface at a distance of 38 cm behind the trailing edge of the short Mylar sheet (no hydrofoil): (*a*) Raw velocity data; (*b*) velocity data after subtracting $U_w(z)$. The solid line is a least squares fit of 2.2.

the mean water surface. The free-surface is at $z' = -a$. The above equation was fitted to the data by determining the wave amplitude that minimized the mean-squared error over the range $-2 > z' > -10$ cm. The resulting velocity perturbation profile, $U_w - U_\infty$, was then subtracted from all the data ($0 \geqslant z' \geqslant -10$ cm). Several of the velocity distributions were also displaced by an amount U_{OS}, where $U_{OS} \approx -0.2$ cm s^{-1} at most, to account for the fact that the distributions after subtracting U_w did not asymptote to the known towing speed, U_∞, see § 3. The reason for this discrepancy between the asymptote and U_∞ is not known. The final distribution after the above processing and displacing the profile upward by the wave amplitude, a, was called the wake velocity distribution and given the symbol $U(z)$:

$$U(z) = \overline{u}(z') - (U_w(z') - U_\infty) - U_{OS},$$

where $\overline{u}(z')$ is the measured data and $z = z' + a$. The wake velocity profile ($U(z)$) corresponding to the raw data in figure 4(*a*) is given in figure 4(*b*).

In order to obtain the surface velocity from the data and to have a mathematical form for the wake velocity profile, an equation given by

$$U(z) = U_\infty \left[1 - q\frac{1 - \tanh(a_1 z^2 + a_2)}{1 - \tanh(a_2)}\right], \quad q = \frac{U_\infty - U(0)}{U_\infty} \tag{2.2}$$

was fitted to the final data $U(z)$, where a_1 and a_2 are fitting parameters. The best set of constants ($U(0)$, a_1 and a_2) for the given velocity data set were determined by minimizing the sum of the squared deviations. (A $\tanh(a_1 z^2)$ profile was used by Mattingly & Criminale (1972) to fit the velocity profiles in the near wake of a hydrofoil and a $\tanh(a_1 z^2 + a_2)$ profile was used by Triantafyllou, Triantafyllou & Chryssostomidis (1986) in the near wake of a cylinder. In the present work, it was found that the latter function gives a smaller average of the squared deviations when fitted to the data.) A curve with the form of (2.2) using the computed constant set has been overlaid on the data in figure 4(*b*). The above data processing was repeated for the three measurement distances for both Mylar sheets giving six velocity profiles (see § 3).

2.3. *Wave-height measurements*

To measure the height of the incipient breaking waves created by the combination of the hydrofoil and the Mylar sheet, it was not possible to use wire gauges fixed to the tank because, in the towing tank, the Mylar sheet would collide with the gauge during the run. Thus, an optical wave-height gauge was used (Lin & Liu 1982). In this device, the beam of a 5W Argon-ion laser (Spectra Physics, model 2017) was pointed vertically down on the water surface at a fixed location in the wave tank. A pair of cylindrical lenses was used to convert the laser beam into a light sheet that was 1mm thick and 8 cm long as it entered the water with the normal to the light sheet directed in the cross-stream direction. The water in the tank was mixed with Fluorescene dye at a concentration of about 1.5 p.p.m so that the water illuminated by the laser glowed with a greenish yellow colour. The intersection of the laser beam and the water surface was observed via a digital linescan camera (*Dalsa Linescan Digital Camera* Model CL-C4 2048A STDJ with a Nikon 200 mm lens). The camera was attached to a vertically oriented linear slide mounted onto a tripod that was fixed to the floor outside the tank. The camera viewed the wave from the side of the tank and above the waterline at approximately a 25° down angle; the plane defined by the line of sight of the camera and the single line of 2048 CCD elements (pixels) was oriented normal to the water surface and perpendicular to the centreplane of the tank. At the plane of the light sheet the array of 2048 pixels covered a physical vertical distance of about 16 cm (0.08 mm per pixel). The CCD elements received little light from the air above the water surface but much more light from the glowing dye at the intersection of the laser light sheet and the water surface. The boundary between the poorly and brightly illuminated CCD elements was taken as the water surface. The camera was set up to record a single line of 2048 eight-bit pixels every 0.004 s. A total of 1.2 s of data was recorded during each experimental run creating an image (vertical distance versus time) of 2048 by 300 pixels. In each image, the water surface was located by an intensity-based thresholding technique. Before any images were taken, a calibration set was created by recording the position of the flat water surface with the camera set at five different heights above the water surface. These heights were known and repeatable through the linear positioner upon which the camera was mounted and gave the relationship between pixel position of the surface image and measured height. Before each set of experimental runs in measuring the waves, a single height image was taken with no wave present to determine the mean water level. In this run and in the calibration runs, it was found that the root-mean-square surface height fluctuation due to mechanical, electronic and data processing noise was about ± 0.006 cm.

At each experimental condition, the profile of the incipient breaking wave was measured in three independent experimental runs. A sample of the three wave profiles for a single experimental condition and the average of the three profiles is given in figure 5. The incipient breaking wave height, ζ_{max}, was taken from the average profile as the vertical distance from the undisturbed water level to the wave crest.

3. Experimental results

In this section, the incipient breaking conditions in terms of the external parameters of the experiment (foil depths and separations distances between the foil and the Mylar sheets) and the wake characteristics as a function of distance behind the trailing edge of the sheet are presented. These results along with the incipient breaking wave amplitudes are discussed in the light of the numerical results and existing theory in § 5.

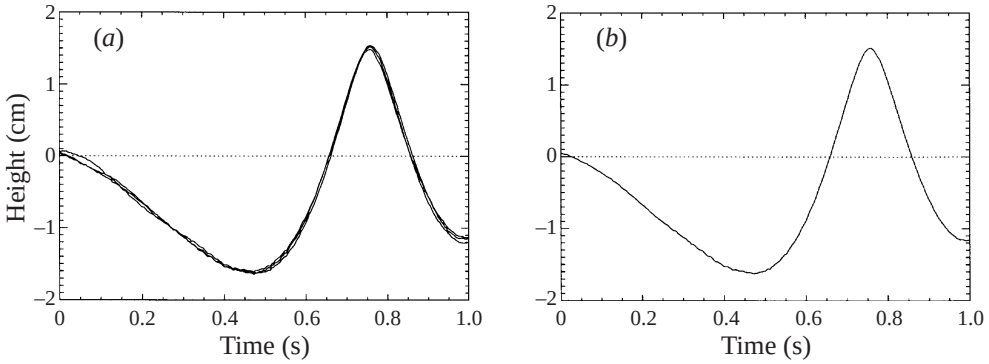

FIGURE 5. Wave-height profiles. (*a*) Profiles for three experimental runs with the same experimental condition, (*b*) average of wave-height profiles in (*a*). Short Mylar sheet, $\Delta x_i = 40\,\text{cm}$, $d = 26.4\,\text{cm}$.

3.1. *Incipient breaking conditions*

Incipient breaking conditions were determined visually through the following procedure. First the depth of submergence of the foil was fixed at a value for which, with no Mylar sheet, the wave did not break. Then the Mylar sheet was put in place and the horizontal separation distance, Δx, between the trailing edge of the Mylar sheet and the leading edge of the hydrofoil was set at a value small enough to cause wave breaking. Over a series of experimental runs, Δx was increased. For large Δx the wake of the sheet at the location of the wave crest is very thick and has a very small surface drift. In this case, the wave behaves much like a wave in calm water, i.e. it does not break. Subsequent runs were used to locate the incipient breaking value of Δx, denoted as Δx_i, which is defined such that for all $\Delta x < \Delta x_i$ the wave breaks. All experiments were performed with the same towing speed, $U_\infty = 80.4\ \text{cm}\,\text{s}^{-1}$. For each Mylar sheet, the value of Δx_i was determined for six depths of submergence. A plot of $\Delta x_i/c$, where c is the chord of the foil, versus d/c, where d is the depth from the undisturbed free-surface to the trailing edge of the foil, is given in figure 6. A separate curve for each Mylar sheet is given in the plot.

3.2. *Wake characteristics*

The wake characteristics (for instance the wake thickness and surface drift velocity) at the location of the incipient breaking wave crest must be determined from the wake velocity distributions which were measured at only three locations in each wake. Thus, characteristics of the mean velocity profiles must be determined by interpolation at places other than the three measurement locations. The mean velocity distributions in the wake at each measuring location as determined by fitting (2.2) to the processed mean velocity measurements as described in § 2.2 are given in figure 7(*a*) for the short Mylar sheet and 7(*b*) for the long Mylar sheet. Wake characteristics taken from these profiles are given in table 2. As can be seen from the plots or the table, the surface drift velocity,

$$q = \frac{U_\infty - U(0)}{U_\infty}, \tag{3.1}$$

decreases and the wake half-thickness, $b_{1/2}$, where

$$\frac{U_\infty - U(z = -b_{1/2})}{U_\infty} = 0.5, \tag{3.2}$$

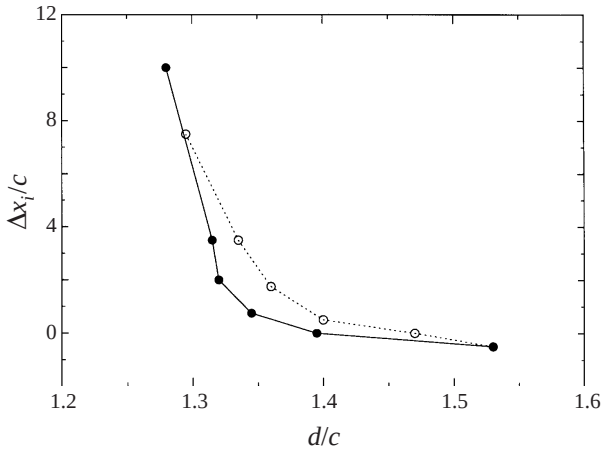

FIGURE 6. Incipient breaking conditions: separation distance between the trailing edge of the Mylar sheet and the leading edge of the hydrofoil, Δx_i, versus the depth of submergence of the trailing edge of the hydrofoil, d, where c is the chord of the hydrofoil. Filled circles: short Mylar sheet, open circles: long Mylar sheet.

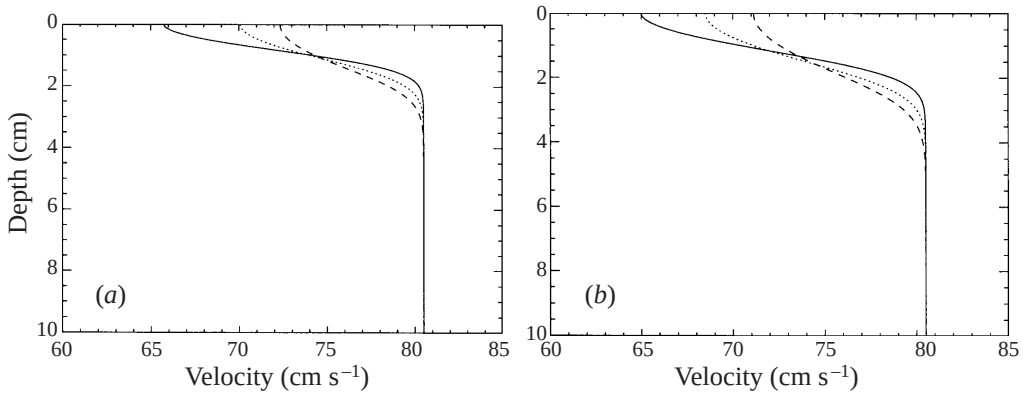

FIGURE 7. Velocity profiles from the fit of Equation 2.2 to the mean velocity measurements: (*a*) short Mylar sheet, (*b*) long Mylar sheet. Shortest streamwise distance ———; middle streamwise distance · · · · · ·; largest streamwise distance – – – – – –.

increases as the distance downstream is increased for both wakes. On the other hand, the momentum thickness,

$$\theta = \int_{-\infty}^{0} \frac{U}{U_\infty}\left(1 - \frac{U}{U_\infty}\right) \mathrm{d}z, \tag{3.3}$$

is (as expected) nearly the same for all three locations in each wake. In the later analysis, the average values of θ for each Mylar sheet, $\theta = 0.145\,\mathrm{cm}$ for the short sheet and $\theta = 0.210\,\mathrm{cm}$ for the long sheet, are used.

For a self-similar wake

$$q = C_1\left(\frac{x - x_1}{\theta}\right)^{-1/2}. \tag{3.4}$$

Using a nonlinear least-squares method, the above equation was fitted to the six data points shown in table 2. The resulting constants were $C_1 = 3.07$ and $x_1 = -47.98\,\mathrm{cm}$

Mylar sheet:	Short			Long		
x (cm)	38	80	120	40	80	120
q	0.184	0.130	0.101	0.193	0.149	0.117
$b_{1/2}$(cm)	0.91	1.22	1.48	1.23	1.58	1.90
θ(cm)	0.150	0.143	0.142	0.210	0.214	0.207
Re_l		4.48×10^5			7.53×10^5	

TABLE 2. Wake characteristics for the short and long Mylar sheets. (x is the streamwise distance from the trailing edge of the sheet to the measurement location. $Re_l = (U_\infty l)/\nu$ is the Reynolds number, where l is the contact length of the sheet and ν is the kinematic viscosity of water.)

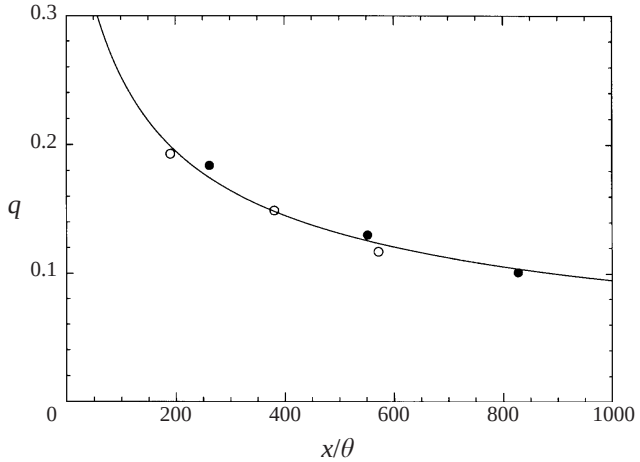

FIGURE 8. Surface drift velocity, q, versus measurement distance, x/θ: ●, short Mylar sheet; ○, long Mylar sheet.

and this curve is plotted along with the data in figure 8. The variation of wake thickness can also be described by a similarity power law defined by

$$\frac{b_{1/2}}{\theta} = C_2 \left(\frac{x - x_2}{\theta} \right)^{1/2}. \tag{3.5}$$

The constants resulting from a nonlinear least-squares fit to the data were $C_2 = 0.34$ and $x_2 = -74.78$ cm and the data along with the curve are shown in figure 9.

4. Numerical simulations

The nonlinear interaction between the surface wake generated by the Mylar sheet and the gravity wave generated by the submerged hydrofoil is also studied numerically considering the following model of the process: (*a*) initially, the sheet wake is modelled as a two-dimensional parallel shear flow and the hydrofoil wave is modelled as a plane gravity wave, and (*b*) the time evolution of their interaction is followed by a direct numerical simulation of the Euler equations.

The velocity profile of the parallel shear flow is identical to the mean velocity profile measured in the wake of the Mylar sheet at a streamwise distance corresponding to the location where the free-surface crosses the mean water level just upstream of the wave crest. As discussed above, the velocity profile of the shear flow is given by (2.2).

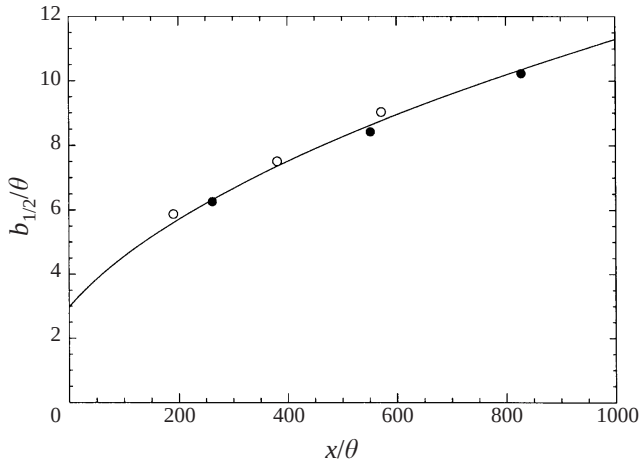

FIGURE 9. Wake thickness, $b_{1/2}/\theta$, versus measurement distance, x/θ: ●, short Mylar sheet; ○, long Mylar sheet.

The plane gravity wave which is added to the shear flow for the initial condition of the numerical model is a second-order periodic Stokes wave with the appropriate wavelength, λ, according to linear theory

$$\lambda = 2\pi \frac{U_\infty^2}{g}. \tag{4.1}$$

The Froude number Fr of the flow, defined as

$$Fr = \frac{U_\infty}{(g b_{1/2})^{1/2}}, \tag{4.2}$$

is related to the dimensionless wavenumber k of a periodic gravity wave according to

$$k = 2\pi \frac{b_{1/2}}{\lambda} = \frac{g b_{1/2}}{U_\infty^2} = \frac{1}{Fr^2}, \tag{4.3}$$

where the characteristic length scale $b_{1/2}$ is the half-width of the velocity profile.

In the following presentation of the equations of motion of the fluid, lengths are non-dimensionalized by $b_{1/2}$ and velocities by U_∞. For a two-dimensional incompressible inviscid free-surface flow, the equations of motion are the continuity equation

$$\frac{\partial u}{\partial x} + \frac{\partial w}{\partial z} = 0 \tag{4.4}$$

and the Euler equations

$$\frac{\partial u}{\partial t} + u\frac{\partial u}{\partial x} + w\frac{\partial u}{\partial z} = -\frac{\partial p}{\partial x}, \tag{4.5}$$

$$\frac{\partial w}{\partial t} + u\frac{\partial w}{\partial x} + w\frac{\partial w}{\partial z} = -\frac{\partial p}{\partial z}, \tag{4.6}$$

where t is time, x, z are the Cartesian coordinates (x is the horizontal coordinate, z is positive in the opposite direction to gravity, and $z = 0$ corresponds to the mean free-surface level), u, w are the velocity components, and p is the dynamic pressure, defined as the pressure P minus the hydrostatic pressure $\left(p = P - \left(-z/Fr^2\right)\right)$. At

the free-surface, the dynamic and kinematic free-surface boundary conditions are, respectively,

$$p = \frac{\eta}{Fr^2} \quad \text{and} \quad w = \frac{\mathrm{d}\eta}{\mathrm{d}t} = \frac{\partial \eta}{\partial t} + u\frac{\partial \eta}{\partial x} \quad \text{at} \quad z = \eta, \tag{4.7}$$

where η is the free-surface elevation and $\mathrm{d}/\mathrm{d}t$ is the total (material) derivative operator.

The free-surface elevation is an unknown function of time, which renders the flow domain time-dependent. Boundary-fitted coordinates are introduced according to the following transformations:

$$x_1 = x, \quad x_2 = z - \eta(x,t), \quad u_1 = u, \quad u_2 = w - \frac{\mathrm{d}\eta}{\mathrm{d}t} = w - \frac{\partial \eta}{\partial t} - u\frac{\partial \eta}{\partial x}, \tag{4.8}$$

where x_i are the coordinates and u_i are the velocity components in the transformed domain.

According to the above transformation, the continuity and the Euler equations, respectively, become (Dimas & Triantafyllou 1994)

$$\frac{\partial u_i}{\partial x_i} = 0, \tag{4.9}$$

$$\frac{\partial u_i}{\partial t} + u_j\frac{\partial u_i}{\partial x_j} = -\frac{\partial p}{\partial x_i} + H_i, \tag{4.10}$$

where

$$H_1 = \frac{\partial p}{\partial x_2}\frac{\partial \eta}{\partial x_1} \quad \text{and} \quad H_2 = \frac{\mathrm{d}^2\eta}{\mathrm{d}t^2}, \tag{4.11}$$

while the dynamic and kinematic free-surface boundary conditions, respectively, become

$$p = \frac{\eta}{Fr^2} \quad \text{and} \quad u_2 = 0 \quad \text{at} \quad x_2 = 0. \tag{4.12}$$

For the direct numerical simulation of the Euler equations, an operator-splitting scheme is employed for the temporal integration and spectral methods for the spatial discretization with Fourier modes along the x_1-direction, and Chebyshev polynomials along the x_2-direction (Dimas 1998). Specifically, 64 Fourier modes were used in the x_1-direction, and 64 Chebyshev modes in the x_2-direction, while the time step was 0.00025. Periodicity boundary conditions are applied in the x_1-direction, while the length of the computational domain in the x_1-direction is equal to the wavelength of the gravity wave. Throughout the computation, fast-Fourier-transform algorithms are used to transform between physical and spectral space, and a spectral preconditioning technique is used on the pressure step of the splitting scheme, which renders the matrix of the resulting system of linear equations banded, thus dramatically reducing the computation time for its solution.

At time $t = 0$, the computation starts with the mean velocity profile and the flow field of the plane gravity wave, while the initial free-surface elevation corresponds to the second-order Stokes wave with an initial wave amplitude η_0, as measured from $z = 0$ to the wave crest.

For this paper, three velocity profiles are considered:

(*a*) $\theta = 1.4\,\mathrm{mm}$, $q = 0.3$, $b_{1/2} \approx 5\,\mathrm{mm}$, $Fr = 3.60$;

(*b*) $\theta = 1.4\,\mathrm{mm}$, $q = 0.2$, $b_{1/2} \approx 7\,\mathrm{mm}$, $Fr = 3.06$;

(*c*) $\theta = 1.4\,\mathrm{mm}$, $q = 0.1$, $b_{1/2} \approx 13\,\mathrm{mm}$, $Fr = 2.25$.

For each velocity profile, the wavelength is evaluated according to (4.3), while several

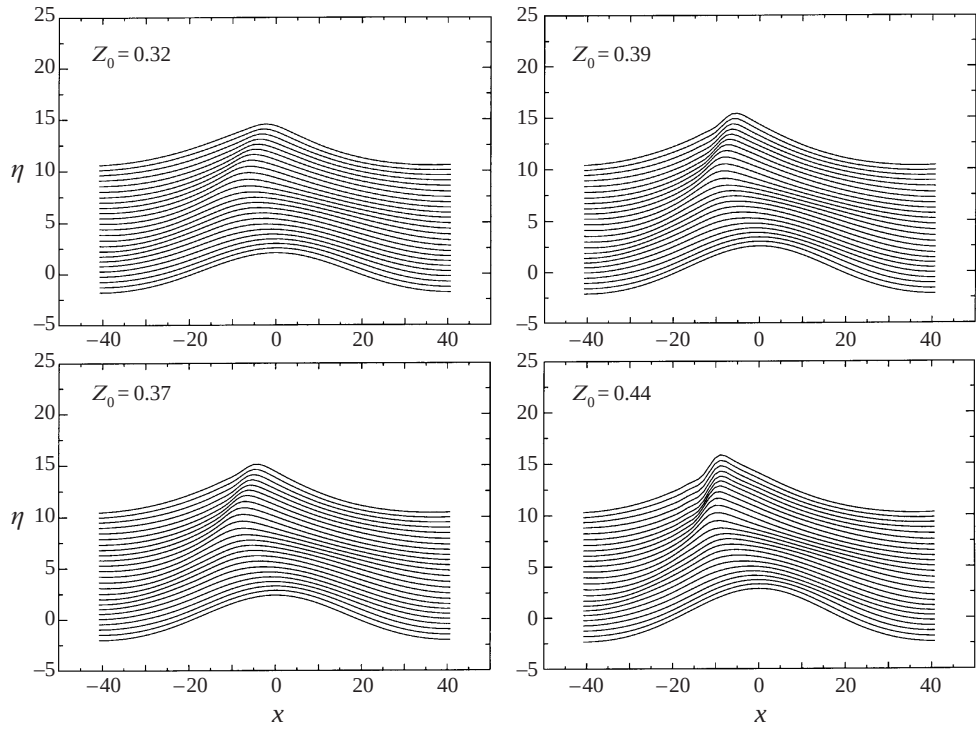

FIGURE 10. Time development of the free-surface elevation, η, for four different initial wave amplitudes, Z_0, and $q = 0.3$. In each case, the free-surface shape is plotted every $\mathrm{d}t = 5$ time units, while for every new curve, the mean water level is shifted upwards by $\mathrm{d}\eta = 0.5$ from that of the previous curve.

dimensionless wave amplitudes η_0 are considered. Results for $q = 0.3$ are presented for $Z_0 = 0.32$, 0.37, 0.39 and 0.44, where Z_0 is defined as

$$Z_0 = \frac{2g\zeta_0}{U_\infty^2} = \frac{2\eta_0}{Fr^2}, \tag{4.13}$$

where $\eta_0 = \zeta_0/b_{1/2}$. For the Stokes limiting wave, $Z_0 = 1.0$ (see (1.1)). The time development of the free-surface elevation for all four cases is shown in a frame of reference moving with the wave phase speed in figure 10. In all cases, after about $t = 20$, the free-surface elevation becomes asymmetric about the wave crest, although the initial condition is symmetric. The level of asymmetry increases as Z_0 is increased. For the highest value, $Z_0 = 0.44$, the free-surface elevation develops a bulge shape on the forward face. This shape is similar to that found in gentle short-wavelength spilling breakers (see Duncan *et al.* 1994, Longuet-Higgins 1996, and Tulin 1996). The point of maximum upward curvature at the leading edge of the bulge is called the toe. To observe the formation of this bulge in the present experiments, it would have been necessary to photograph the transition of the wave from a non-breaking to a breaking state as the hydrofoil started from rest. These measurements were not attempted. For the case with $Z_0 = 0.44$, vorticity contour plots of the flow at four time instants around the time of the bulge formation are shown in figure 11. Note that the vorticity field has a smooth spatial distribution up to the moment of bulge formation at about $t = 80$ which results in an instability of the vorticity field. The instability is localized in the area of the toe at $x \approx -12$ and is associated with the

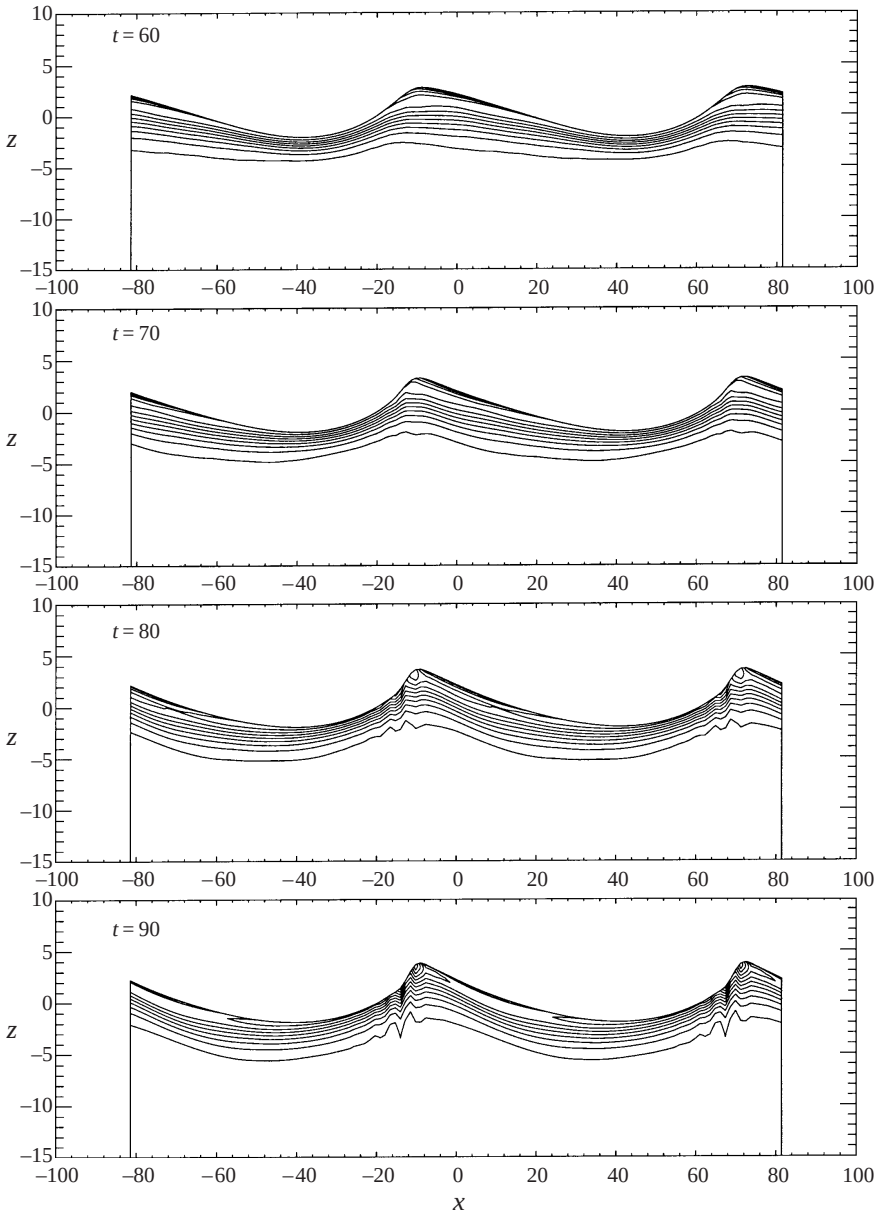

FIGURE 11. Vorticity contour plots of the flow at four time instants around the time of the bulge formation for $Z_0 = 0.44$ and $q = 0.3$. Solid contours correspond to negative vorticity, broken contours correspond to positive vorticity, and the increment between contours is 0.02.

sharp variation of the free-surface slope. A computation with 128 Fourier modes (256 grid points) in the x_1-direction exhibits the same instability, since this sharp shape of the free-surface at the toe of the bulge cannot be resolved with any finite number of modes. On the other hand for the case $Z_0 = 0.32$, there is no bulge formation during the free-surface development and the vorticity distribution remains smooth as seen in figure 12. As discussed in the following section, these differences in the vorticity field are used to define incipient breaking conditions in the numerical results.

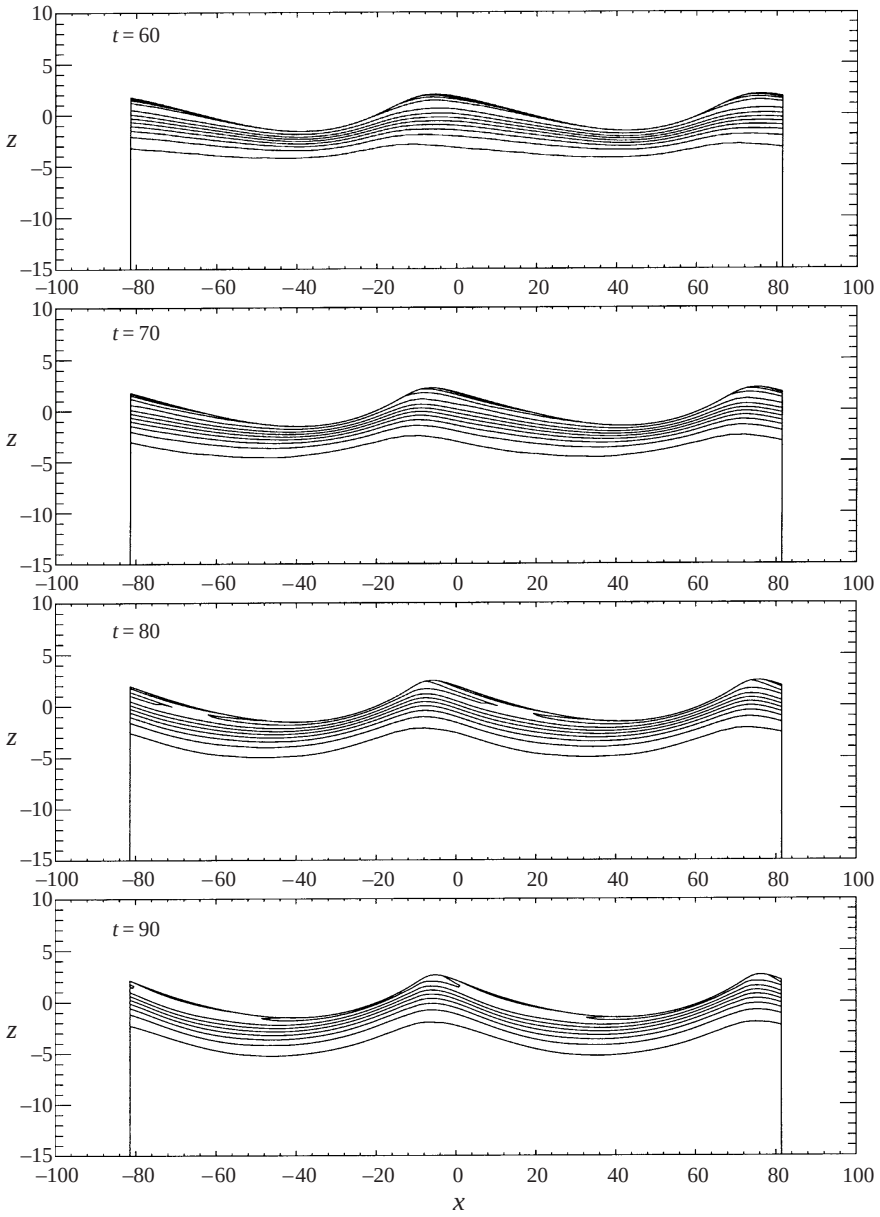

FIGURE 12. Vorticity contour plots of the flow at four time instants for $Z_0 = 0.32$ and $q = 0.3$. Solid contours correspond to negative vorticity, broken contours correspond to positive vorticity, and the increment between contours is 0.02.

5. Discussion

To examine the effect of the surface wake on the experimentally determined incipient breaking conditions, the dimensionless incipient wave amplitude, $Z_{max} = 2g\zeta_{max}/U_\infty^2$, is plotted versus the dimensionless drift velocity, q, in figure 13. The values of ζ_{max} were taken from the profile measurements at the 12 incipient breaking conditions plotted in figure 6. The corresponding values of q were taken from (3.4) with the measured value of θ for each wake and the streamwise location behind the sheet taken at the point

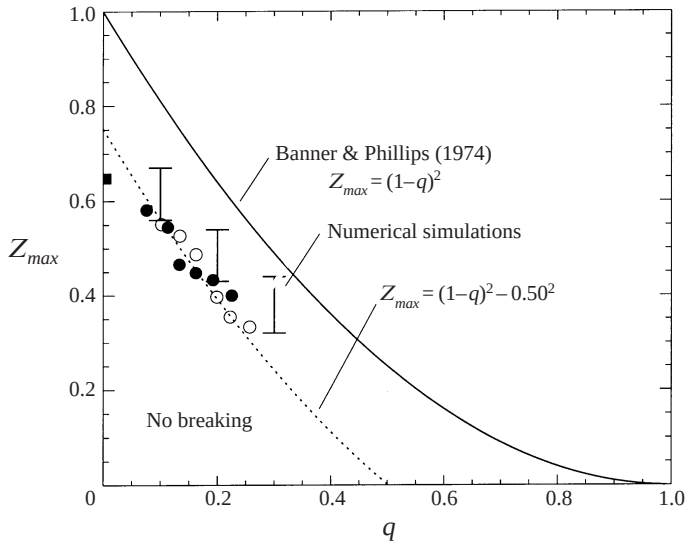

FIGURE 13. Non-dimensional wave amplitude versus local drift velocity at incipient breaking conditions: ●, short Mylar sheet; ○, long Mylar sheet; ■, data from Duncan (1983); ——, theory of Banner & Phillips (1974); ....., modified theory (see (5.1)). The bars are from the present numerical calculations: top horizontal line is definitely unstable, bottom horizontal line is definitely stable.

where the water surface profile crossed the mean water level just upstream of the wave crest. (Varying this distance back to the crest location did not change the results significantly.) The values of q thus obtained are directly comparable to the definition of the surface drift in Banner & Phillips (1974). As can be seen from the figure, the experimental data for both the long and short Mylar sheets follow a single curve. This indicates that the variations in wake momentum thickness (for $\theta = 0.145$ cm and 0.210 cm or $\theta/\lambda = 0.0035$ and 0.0051, respectively) have little effect on the incipient breaking amplitude for the single towing speed used here, 80.4 cm s^{-1}. The data point plotted at $q = 0$ is from Duncan (1983) for a steady wave moving in calm water. Waves with amplitudes a little higher than this value will form a steady breaker if disturbed from equilibrium for a short time (see § 1).

Also plotted in figure 13 is a curve showing the theoretical result due to Banner & Phillips (1974). The shape of this curve is similar to that of the experimental data, but the magnitude is considerably higher. With this in mind, the theory of Banner & Phillips (1974) is modified herein such that the incipient breaking condition is defined as the wave amplitude for which the fluid velocity at the crest is αU_∞, where the factor α is to be determined from the experimental data. The resulting modified form of (1.2) is

$$Z_{max} = (1-q)^2 - \alpha^2. \tag{5.1}$$

From a least-squares fit to the experimental data (including the point from Duncan 1983), α was found to equal 0.50 and the resulting curve is plotted as a dotted line in figure 13. This modified theory overestimates the wave height at $q = 0$ but is otherwise a fairly good fit to the data. If this theory is assumed to be accurate, it would indicate that incipient breaking occurs in the presence of a surface wake when the fluid particle speed at the crest reaches 50% of the wave phase speed.

Our numerical simulations indicate that the time evolution of the fluid velocity

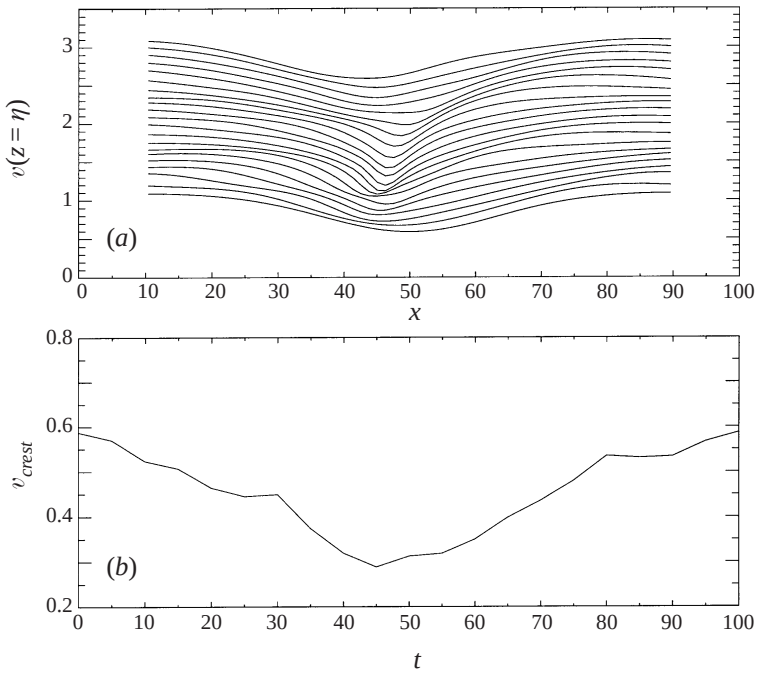

FIGURE 14. Time development of (*a*) the free-surface fluid velocity magnitude and (*b*) the crest velocity magnitude for $Z_0 = 0.64$ and $q = 0.1$. In (*a*), each curve is plotted every $\mathrm{d}t = 5$ time units and it is shifted upwards by $\mathrm{d}v = 0.1$ from the previous curve.

at the crest reaches a minimum value during the bulge formation. As an example, for $q = 0.1$ and $Z_0 = 0.64$, the time development of the fluid velocity magnitude, $v = (u^2 + w^2)^{1/2}$, along the free-surface is shown in figure 14. As can be seen from the figure, the fluid velocity magnitude at the crest reaches a minimum at about $t = 45$ during the bulge formation. This minimum value of the crest fluid velocity is a function of the drift velocity, q, and the dimensionless parameter Z_0. For values of Z_0 along the dotted line of figure 13 the minimum crest velocity is not equal to $0.5U_\infty$ as predicted by the modified theory of Banner & Phillips (1974). In fact, the minimum crest velocity varies from about $0.3U_\infty$ for $q = 0.1$ to about $0.5U_\infty$ for $q = 0.3$. This difference between our numerical model and the theory of Banner & Phillips (1974) arises from the fact that our model includes the unsteady nonlinear evolution of the wake layer and its vorticity field.

At incipient breaking conditions, an instability appears to develop at the toe of the wave as discussed in the previous section. For a given value of q, we define a range for the wave amplitude parameter Z_0 in the following manner. The lower limit of the range corresponds to the maximum initial amplitude of the gravity wave for which no instability develops at the toe of the wave during the simulation, indicating no breaking. This boundary should be directly comparable to the experimentally determined incipient breaking condition. The upper limit of the range corresponds to the minimum initial wave amplitude for which a strong instability originates at the toe of the wave, indicating a definite breaking condition. These numerically determined boundaries are plotted in figure 13 and are in good agreement with the experimental data.

6. Conclusions

The experiments and numerical simulations reported herein indicate that, as proposed by Banner & Phillips (1974), the maximum amplitudes of steady non-breaking water waves are reduced in the presence of a surface drift layer that flows in the direction of wave propagation, and the reduction increases with increasing drift velocity. Our results, though, indicate that these maximum heights are much smaller than the ones predicted by Banner & Phillips (1974) whose breaking criterion is based on the assumption of zero fluid velocity at the wave crest in the frame of reference moving with the crest. For example, for the highest surface drift velocity used herein, $q = 0.27$, our incipient breaking height is about 60% of the one predicted by Banner & Phillips (1974) and about 33% of the Stokes' wave limiting height. Our incipient breaking heights are independent of the wake momentum thickness over the range from $\theta =$ 0.145 cm to 0.210 cm ($\lambda/\theta = 286$ to 197, where $\lambda = U_\infty^2/(2\pi g)$ is the wavelength from linear theory in calm water). The numerical simulations show that breaking is associated with the formation of a bulge on the forward face of the crest of the wave and a point of high upward curvature (called the toe) at the leading edge of this bulge. For large enough wave steepness, it is observed that vorticity fluctuations increase dramatically just under the surface in this region of the flow. The incipient breaking amplitudes based on whether or not this local growth of vorticity fluctuations occurs are in good agreement with the experimental data.

From the experimental measurements and theoretical analysis like that of Banner & Phillips (1974), it was found that the crest fluid velocity at the incipient breaking condition in the reference frame of the crest is 50% of the wave phase speed, U_∞, relative to the water at infinite depth. Our numerical simulations, though, indicate that the crest fluid velocity for incipient breaking conditions varies from $0.3U_\infty$ for lower drift velocities to $0.5U_\infty$ for higher velocities. The difference between these values of the crest fluid velocity and those from the combined experimental data and theoretical analysis mentioned above is assumed to be due to the inclusion of the unsteady nonlinear evolution of the wake layer and its vorticity field in the numerical calculations.

It is concluded, therefore, that the incipient wave height is lower than the one predicted by Banner & Phillips (1974) due to the vorticity action in the toe region, which renders the use of a zero-crest-velocity criterion impractical to characterize incipient breaking conditions.

The support of the Office of Naval Research under contracts N000149610368 and N000149610940, Program Officer Dr Edwin P. Rood, is gratefully acknowledged.

REFERENCES

Banner, M. L. & Phillips, O. M. 1974 On the incipient breaking of small scale waves. *J. Fluid Mech.* **65**, 647–656.

Battjes, J. A. & Sakai, T. 1981 Velocity field in a steady breaker. *J. Fluid Mech.* **111**, 421–437.

Dimas, A. A. 1998 Free-surface wave generation by a fully-submerged wake. *Wave Motion* **27**, 43–54.

Dimas, A. A. & Triantafyllou, G. S. 1994 Nonlinear interaction of shear flow with a free-surface. *J. Fluid Mech.* **260**, 211–246.

Duncan, J. H. 1981 An experimental investigation of breaking waves produced by a towed hydrofoil. *Proc. R. Soc. Lond.* **377**, 331–348.

Duncan, J. H. 1983 The breaking and non-breaking resistance of a two-dimensional hydrofoil. *J. Fluid Mech.* **126**, 507–520.

Duncan, J. H., Qiao, H., Behres, M. & Kimmel, J. 1994 The formation of a spilling breaker. *Phys. Fluids* **6**, 2558–2560.

Lamb, H. 1932 *Hydrodynamics*. Dover.

Lin, J.-T. & Liu, H.-T. 1982 On the spectra of high-frequency wind waves. *J. Fluid Mech.* **123**, 165–185.

Longuet-Higgins, M. S. 1996 Progress towards understanding how waves break. Presented at *21st Symp. on Naval Hydrodynamics, Trondheim, Norway, June 24–28*.

Mattingly, G. E. & Criminale, W. O. 1972 The stability of an incompressible two-dimensional wake. *J. Fluid Mech.* **51**, 233–272.

Miche, M. R. 1944 Mouvements ondulatories de la mer en profundeur constante ou décroisante. *Annales des Ponts et Chaussées* **114**, 25–87, 131–164, 270–292, 396–406. English translation: *Institute for Engineering Research, Wave Research Laboratory, University of California at Berkeley*, Series 3, Issue 363, 1954.

Parker, F. 1994 The Royal Navy's Boxer. *Proc. US Naval Institute* **120**, part 3, Cover.

Salvesen, N. 1981 Five years of numerical naval ship hydrodynamics at DTNSRDC. *J. Ship Res.* **25**, 219–235.

Salvesen, N. & Kerczek, C. von 1976 Nonlinear aspects of free-surface flow past two-dimensional bodies. *14th IUTAM Delft*.

Simmen, J. A. & Saffman, P. G. 1985 Steady deep-water waves on a linear shear current. *Stud. Appl. Maths* **73**, 35–57.

Stokes, G. G. 1847 On the theory of oscillatory waves. *Trans. Camb. Phil. Soc.* **8**, 441.

Teles Da Silva, A. F. & Peregrine, D. H. 1988 Steep, steady surface waves on water of finite depth with constant vorticity. *J. Fluid Mech.* **195**, 281–302.

Triantafyllou, G. S., Triantafyllou, M. S. & Chryssostomidis, C. 1986 On the formation of vortex streets behind stationary cylinders. *J. Fluid Mech.* **170**, 461–477.

Tulin, M. P. 1996 Breaking of ocean waves and downshifting. In *Waves and Nonlinear Processes in Hydrodynamics*, pp. 177–190. Kluwer.